nature geoscience

Article

https://doi.org/10.1038/s41561-023-01250-y

Benthic δ¹⁸O records Earth's energy imbalance

Received: 19 October 2022

Accepted: 13 July 2023

Published online: 31 August 2023



Check for updates

Sarah Shackleton ¹ □, Alan Seltzer ², Daniel Baggenstos ^{3,4} & Lorraine E. Lisiecki © 5

Oxygen isotope ratios (δ^{18} O) of foraminifera in marine sediment records have fundamentally shaped our understanding of the ice ages and global climate change. Interpretation of these records has, however, been challenging because they reflect contributions from both ocean temperature and ice volume. Here, instead of disentangling, we reconstruct global benthic foraminiferal δ^{18} O across the last deglaciation (18–11.5 ka) with ice volume constraints from fossil corals and ocean temperature constraints from ice core noble gases. We demonstrate that, while ocean temperature and ice volume histories are distinct, their summed contributions to δ^{18} O agree remarkably well with benthic δ^{18} O records. Given the agreement between predicted and observed δ^{18} O, we further build upon recent insight into global energy fluxes and introduce a framework to quantitively reconstruct top-of-atmosphere net radiative imbalance, or Earth's energy imbalance, from δ^{18} O. Finally, we reconstruct 150,000 years of energy imbalance, which broadly follows Northern Hemisphere summer insolation but shows millennial-scale energy gain during the cold intervals surrounding Heinrich events. This suggests that, in addition to external forcing, internal variability plays an important role in modifying the global energy budget on long (millennial-plus) timescales.

Among the geochemical tools used to inform our understanding of global climate over the past 100 million years, the oxygen isotope ratio $(\delta^{18}O)$ of benthic foraminifera in marine sediment cores has arguably provided the foremost insights into the structure of past climate oscillations, fundamentally shaping the field of palaeoclimatology over the past 70 years^{1,2}. Initially interpreted as a proxy for ocean temperature³, it was later argued that Pleistocene for a miniferal δ^{18} O primarily records changes in seawater δ^{18} O, and thus global ice volume (or sea level), due to the growth and decay of 18O-depleted ice sheets4.

Several decades after these early interpretations of foraminiferal δ^{18} O records, it was recognized that marine sediment porewaters provide direct constraints on past seawater $\delta^{18}O$ (ref. 5). Porewater $\delta^{18}O$ profiles indicate a 1.0 ± 0.1% global average seawater enrichment during the Last Glacial Maximum (LGM; ref. 6 and references therein), suggesting that roughly 60% of the 1.7% LGM global benthic δ^{18} O $(\delta^{18}O_{henth})$ anomaly was due to changes in ice volume, with the remainder due to the influence of colder deep ocean temperatures on the calcification process. However, the relative contributions of ice volume and ocean temperature to δ^{18} O_{benth} evolve in time, and disentangling these signals is key to our understanding of the ice ages^{7–13}.

While the separation of $\delta^{18}O_{benth}$ into ocean temperature and ice volume has been a major focus of prior work, the combined signals provide powerful constraints on the global energy budget. Today our energy budget is imbalanced, with more energy coming in than escaping to space, driven by anthropogenic changes to our atmosphere¹⁴. Earth's energy imbalance (EEI) determines how the climate evolves

¹Department of Geosciences, Princeton University, Princeton, NJ, USA. ²Marine Chemistry and Geochemistry Department, Woods Hole Oceanographic Institution, Woods Hole, MA, USA. 3 Australian Antarctic Division, Kingston, Tasmania, Australia. 4 Australian Antarctic Program Partnership, Institute for Marine and Antarctic Studies, University of Tasmania, Hobart, Tasmania, Australia. 5Department of Earth Science, University of California Santa Barbara, Santa Barbara, CA, USA. Se-mail: ss77@princeton.edu

and is closely linked to equilibrium climate sensitivity¹⁵. The response of EEI to natural forcing and unforced internal variability provides insight into global climate feedbacks.

Recent work has demonstrated that the global energy gains associated with ocean warming and ice sheet melting across the last deglaciation are (1) similar in magnitude, and (2) dominate the net deglacial energy change ¹⁶. Using eustatic sea level ¹⁷ and global mean ocean temperature reconstructions ^{16,18}, ref. 16 quantified total deglacial energy changes associated with the latent heat of ice sheet melting and ocean heat uptake. By conservation of energy, the rate of global heat uptake/release must equal the EEI. Therefore, the reconstructed rate of global energy gain was used to reconstruct EEI from the LGM to present.

Given that $\delta^{18}O_{benth}$ contains ocean temperature and ice volume information, it may unlock unique insight into past global energy changes and EEI. However, this requires that (1) $\delta^{18}O_{benth}$ reliably records combined ocean temperature and ice volume changes, and (2) we can quantitatively translate $\delta^{18}O_{benth}$ changes into global energy changes. In this Article, we explore the potential of $\delta^{18}O_{benth}$ as a proxy for global energy by comparing ocean temperature, ice volume and $\delta^{18}O_{benth}$ records over the last 25,000 years. We then consider the implications for the global energy budget within and beyond this interval.

LGM to present ocean temperature and ice volume constraints

The histories of ocean temperature and ice volume from the LGM through the present (25–0 ka) provide crucial insight into the climate's response to extensive changes in the global energy budget. While relatively sparse for earlier intervals, numerous constraints on ocean temperature and ice volume exist for the last 25,000 years.

Fossil coral and sediment-based constraints on tidal range provide information on relative sea level change. However, relative sea level changes are influenced by multiple factors including ocean/ice volume, and the deformation of Earth's crust and gravitational field in response to the redistribution of ice masses (or glacio-isostatic adjustment). Recent advances in constraining LGM-to-present ocean/ice volume histories have relied on combined relative sea level observations and glacio-isostatic adjustment models (for example, ref. 17).

Our understanding of past ocean temperature is primarily based on marine geochemical records. However, most marine proxies record sea surface temperatures, which represent a small fraction of the ocean. Recent work demonstrated that atmospheric noble gas ratios (Xe/N₂, Kr/N₂ and Xe/Kr) in ice core air bubbles reflect mean ocean temperature Because the temperature-dependent solubilities of xenon, krypton and nitrogen in seawater are distinct, ocean warming or cooling modifies the ocean–atmosphere partitioning of these gases in different proportions, therefore modifying atmospheric Xe/N₂, Kr/N₂ and Xe/Kr. Multiple noble-gas-based deglacial records of ocean temperature have been produced 16,18,20 and closely agree, thus bolstering confidence in the method (Extended Data Fig. 1).

Comparing predicted and observed δ¹⁸O histories

The individual contributions of ocean temperature and ice volume to $\delta^{18}O_{benth}$, their sum, and a global $\delta^{18}O_{benth}$ compilation 21 are compared in Fig. 1 (Methods). Here we report $\delta^{18}O_{benth}$ anomalies $(\Delta\delta^{18}O)$ relative to the last 5,000 years. For brevity we refer to the $\delta^{18}O_{benth}$ compilation as $\Delta\delta^{18}O_{observed}$ and the sum of ocean temperature and ice volume-derived $\Delta\delta^{18}O$ as $\Delta\delta^{18}O_{predicted}$. The overall agreement between $\Delta\delta^{18}O_{predicted}$ and $\Delta\delta^{18}O_{observed}$ is quite striking considering the distinct evolutions of the ocean temperature and ice volume contributions. However, the magnitude of LGM-to-Holocene $\Delta\delta^{18}O_{predicted}$ exceeds that of $\Delta\delta^{18}O_{observed}$. Another notable difference is the timing of the LGM $\Delta\delta^{18}O$ maximum, which occurs earlier (-22 ka) in $\Delta\delta^{18}O_{predicted}$ than in $\Delta\delta^{18}O_{observed}$ (-19 ka). In agreement with previous work 6,8 , ocean temperature and ice volume changes respectively make up roughly 40% and 60% of the total LGM (25–18 ka) $\Delta\delta^{18}O$.

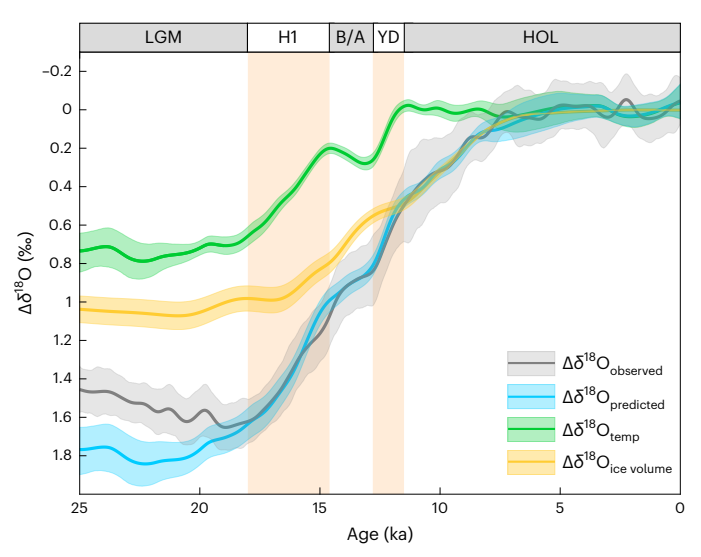


Fig. 1| **Contributions of ocean temperature and ice volume changes to global** $\Delta \delta^{18} O$. The green and yellow splines show predicted temperature and ice volume contributions to $\Delta \delta^{18} O$, respectively. The ocean temperature contribution is calculated using a compilation of atmospheric noble gas reconstructions 16,18,20,40 and the ice volume contribution is calculated using the ref. 17 eustatic sea level reconstruction, assuming a mean ice sheet $\delta^{18} O$ of $-30 \pm 2\%$ (Methods). The blue spline is the sum of the temperature and ice volume contributions ($\Delta \delta^{18} O_{\text{predicted}}$) compared with the global $\delta^{18} O_{\text{benth}}$ compilation 21 ($\Delta \delta^{18} O_{\text{observed}}$, grey). Shading indicates the 1σ uncertainty of the reconstructions centred on the mean (solid line). Orange panels highlight H1 (18–14.6 ka) and the YD (12.8–11.5 ka). LGM (25–19 ka), B/A (14.6–12.8 ka) and Holocene (HOL, 11.5–0 ka) intervals are also denoted in the top panel.

Within the deglaciation (18–11.5 ka) and Holocene, we observe excellent agreement between $\Delta \delta^{18}O_{predicted}$ and $\Delta \delta^{18}O_{observed}$. Both show highest rates of $\Delta \delta^{18}O$ change during Heinrich Stadial 1 (H1, 18–14.6 ka) and the Younger Dryas (YD, 12.8–11.5 ka), with a notable inflection during the Bølling–Allerød (B/A, 14.6-12.8 ka). During H1, the majority (0.5‰) of $\Delta \delta^{18}O$ (0.6‰) may be attributed to a 1.7 °C mean ocean warming. During the B/A, ocean temperatures cool which, alone, would lead to a reversal in $\Delta \delta^{18}O$. However, the highest rates of ice sheet melting occur within this interval; the net effect is the observed inflection. As in H1, the high rate of $\Delta \delta^{18}O$ change in the YD is primarily driven by ocean warming. The $\Delta \delta^{18}O$ in the early Holocene (0.5‰,11.5–8 ka) is entirely explained by the melting of residual LGM ice sheets, as ocean temperatures stabilize by the onset of the Holocene.

Disagreement in LGM $\Delta\delta^{18}O$

Given the excellent agreement between $\Delta\delta^{18}O_{predicted}$ and $\Delta\delta^{18}O_{observed}$ within the deglaciation and Holocene, the disagreement in both the magnitude and trend of LGM $\Delta\delta^{18}O$ is notable. Multiple explanations could resolve this misfit. First, the larger magnitude of LGM-to-Holocene $\Delta\delta^{18}O_{predicted}$ may indicate that the mean ice sheet $\delta^{18}O$ ($\delta^{18}O_{ice}$) applied in our calculations (–30%) is too negative (Fig. 2a). The choice of an invariant $\delta^{18}O_{ice}$ in these calculations is a simplifying assumption; ice sheet $\delta^{18}O$ is spatially heterogeneous and varies as a function of temperature, latitude and altitude 22 . We therefore expect $\delta^{18}O_{ice}$ to evolve as a function of lateral and vertical ice sheet extent and global temperature. To explain the discrepancy between $\Delta\delta^{18}O_{predicted}$ and $\Delta\delta^{18}O_{observed}$ with evolving $\delta^{18}O_{ice}$ requires an 8% decrease in $\delta^{18}O_{ice}$ between 25 ka and 19 ka. Given that the reconstructed ice volume 17 and global temperatures 23 are quite stable during this interval, this scenario is not well supported.

The discrepancy may also be explained by a smaller ocean temperature change than suggested by the noble-gas-based reconstruction. Today, the deep ocean is undersaturated in krypton and xenon²⁴.

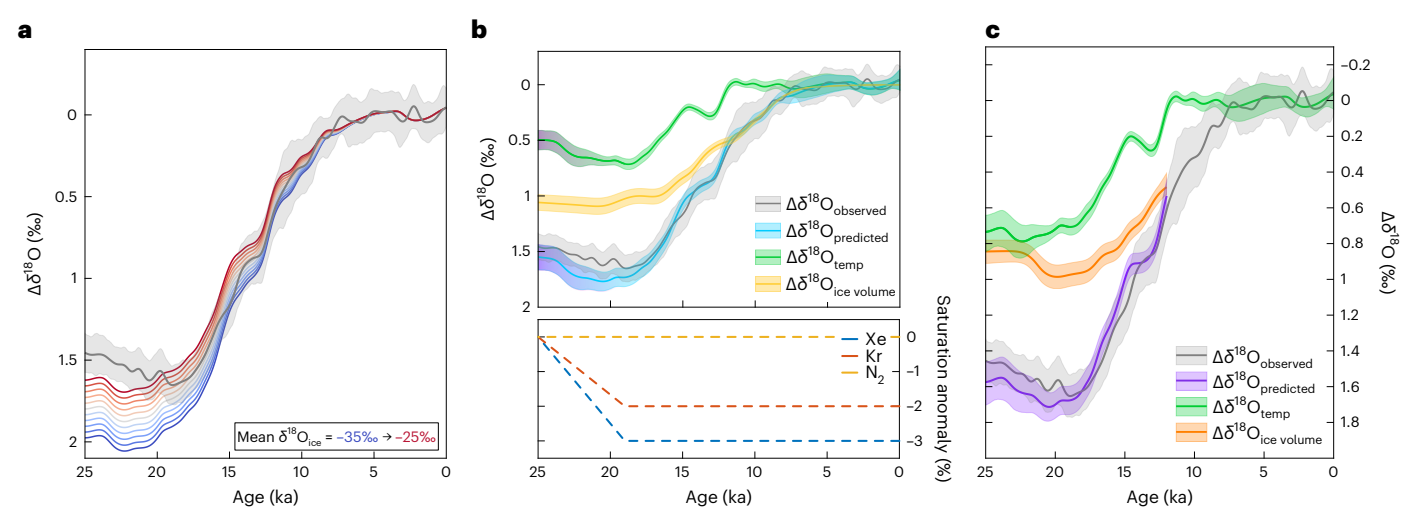


Fig. 2 | Sensitivity of LGM $\Delta\delta^{18}O_{predicted}$ to mean $\delta^{18}O_{ice}$, noble gas saturation state and applied sea level reconstruction. a, A range (–25% to –35%) of mean $\delta^{18}O_{ice}$ values are used to calculate $\Delta\delta^{18}O_{predicted}$ to test the sensitivity of this parameter in the calculation of the relative contribution of ice volume changes to the evolution of $\Delta\delta^{18}O_{predicted}$. b, We prescribe a noble gas saturation scenario (bottom) to calculate the ocean temperature contribution to $\Delta\delta^{18}O_{predicted}$ from atmospheric noble gas reconstructions 16,18,20,40 to fit the $\Delta\delta^{18}O_{observed}$ (top, ref. 21). Noble gases are prescribed at 100% saturation at 25 ka, and then

linearly adjusted to their mean modern values ²⁴ between 25 ka and 19 ka. Purple shading in top panel indicates where the prescribed saturation changes are applied. \mathbf{c} , We evaluate the LGM ice volume $\Delta \delta^{18}$ O contribution (orange) and $\Delta \delta^{18}$ O predicted (purple) applying the ref. 29 eustatic sea level reconstruction. This reconstruction is limited to 32–12 ka. Comparisons of the raw sea level data and eustatic sea level curves of refs. 17,29 are shown in Extended Data Fig. 2. As in Fig. 1, spline shadings in all three panels shows the 1σ uncertainty centred on the mean (solid lines).

Differences between LGM and Holocene ocean boundary conditions including sea ice extent, wind stress, circulation and meridional temperature gradients may have resulted in different noble gas saturation states. If the LGM ocean were less undersaturated in krypton and xenon, this would result in an overestimate of the LGM-to-Holocene ocean temperature change and its contribution to $\Delta \delta 18O_{predicted}^{25}$. For undersaturation to explain the discrepancy would require a contemporaneous decrease in ocean temperature and increase in noble gas undersaturation between 25 ka and 19 ka, followed by minimal changes in saturation state across the deglaciation and Holocene (Fig. 2b). Given the evidence for relatively stable LGM sea ice extent, wind stress, ocean circulation and meridional temperature gradients, followed by large changes in these parameters during the deglaciation 23 , this scenario is not well supported.

Last, we consider an alternative LGM ice volume history. The timing and magnitude of the LGM sea level minimum has been widely debated, as constraints on sea level in this interval are sparse (Extended Data Fig. 2) and often inconsistent with land-based ice volume estimates $^{26-28}$. Recently, an LGM eustatic sea level history was constructed with drowned corals from the Great Barrier Reef 29 . The reconstruction suggests ice volume reached a maximum at -19 ka, immediately preceding the deglaciation. Applying this reconstruction to calculate LGM $\Delta \delta^{18}O_{predicted}$, we find substantially improved agreement with $\Delta \delta^{18}O_{observed}$ in the overall magnitude and trend (Fig. 2c). We note that there may be other explanations for this mismatch, including the potential of diagenesis to alter $\delta^{18}O_{benth}$ records 30 . However, of the proposed explanations, we favour this late drop in LGM sea level to explain the $\Delta \delta^{18}O_{predicted}$ misfit, which indicates that the $\delta^{18}O_{benth}$ maximum at 19 ka records the true LGM ice volume maximum.

$\delta^{18}O_{benth}$ as a proxy for EEI

Because $\delta^{18}O_{benth}$ reliably records combined ocean temperature and ice volume information, it should track net energy changes associated with ocean warming/cooling (ocean heat content) and ice sheet buildup/melting (latent heat content). As these are the dominant energy reservoirs of the ice ages 16 , $\delta^{18}O_{benth}$ may serve as a direct tracer of global net energy changes (ΔE_{global}) and EEI. However, to quantitatively reconstruct

 ΔE_{global} and EEI from $\delta^{18}O_{benth}$ requires that (1) $\delta^{18}O_{benth}$ is reliably separated into its two components, or (2) a given $\delta^{18}O_{benth}$ change associated with ocean temperature or ice volume results in a similar total energy change. Remarkably, the latter is upheld. That is, the total energy change associated with a given change in $\delta^{18}O_{benth}$ if it were entirely attributed to ocean warming/cooling (19 \times 10 24 J ** 0) or entirely to ice sheet melting/fusion (16 \times 10 24 J ** 0 are remarkably similar (Extended Data Figs. 3 and 4).

In this context, there is no need to deconstruct $\delta^{18}O_{benth}$; it can be directly translated into ΔE_{global} without accurate knowledge of its partitioning between the oceans and ice sheets. $\delta^{18}O_{benth}$ therefore serves as an agnostic tracer of ΔE_{global} and EEI. As a test of this novel interpretation, we apply this agnostic $\delta^{18}O_{benth}^{}-\Delta E_{global}^{}$ conversion to the ref. 21 compilation, reconstruct deglacial EEI from its time derivative, and compare results with diagnostic EEI reconstructed from combined ocean and latent heat changes (Fig. 3a,b). While minor differences exist, the key features are the same; EEI contains two peaks within the last deglaciation, coincident with H1 and the YD.

We may therefore extend EEI reconstructions further into the past with $\delta^{18}O_{benth}$. EEI reconstructed from the ref. 21 global compilation suggests that the majority of the last glacial (116–19 ka) has modestly negative EEI associated with gradual cooling and ice sheet growth (Fig. 3c). However, this interval is punctuated by a number of EEI peaks that correspond to cold intervals (stadials) in which Heinrich events—times of extensive ice rafted debris deposition in the North Atlantic—occur³¹. Heinrich Stadials (H) are associated with substantial reduction in Atlantic Meridional Overturning Circulation (AMOC) 32,33 and drastically reduced surface temperatures in the Northern Hemisphere. It is hence not obvious why these cold periods coincide with positive EEI anomalies.

Climate simulations of AMOC disruptions suggest that the radiative response is dominated by two opposing effects: (1) an increase in albedo and outgoing shortwave radiation due to the expansion of North Hemisphere sea ice and low level clouds, and (2) a decrease in outgoing longwave radiation due to strong Northern Hemisphere surface and atmospheric cooling³⁴. The simulated magnitude of the longwave response outweighs the shortwave, leading to a positive EEI,

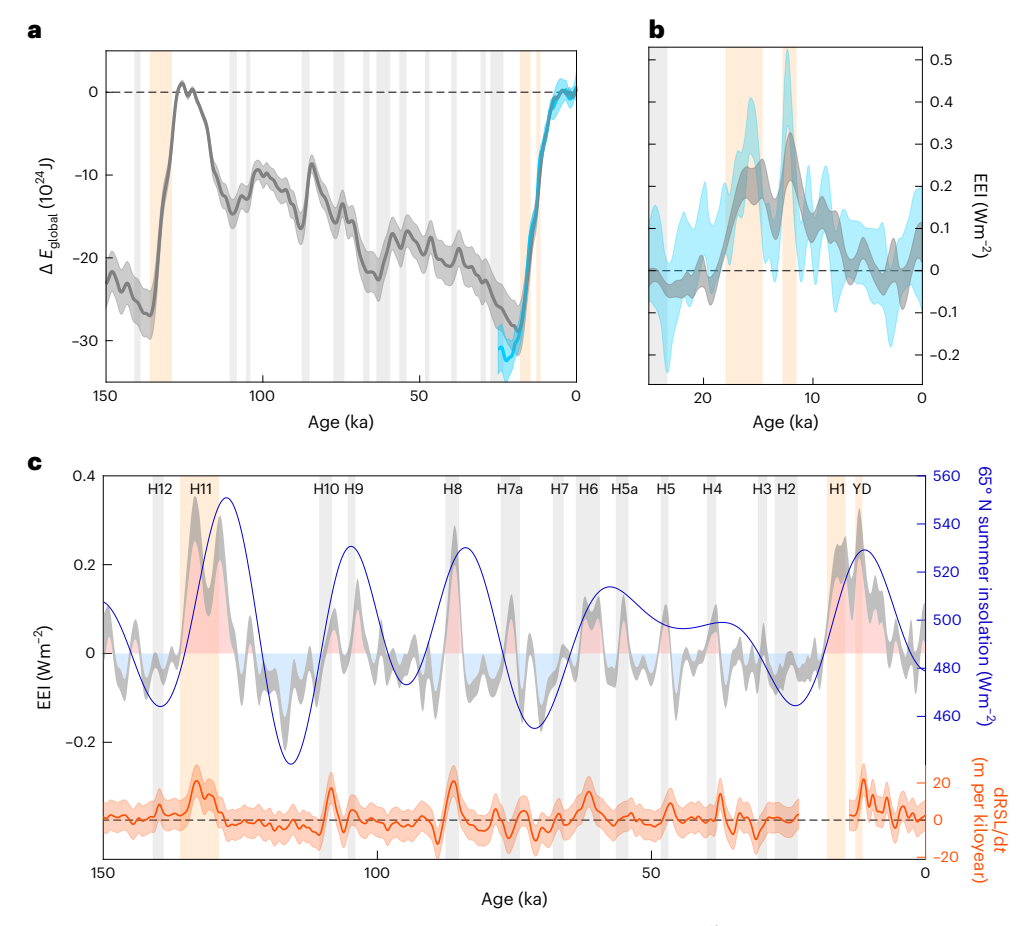


Fig. 3 | Global energy change ($\Delta E_{\rm global}$) and EEI on a range of timescales. a, $\Delta E_{\rm global}$ over the last 150 kiloyears calculated from $\delta^{\rm I8}{\rm O}_{\rm benth}$ (ref. 21) (grey) compared with calculation using constraints from combined changes in ocean and latent heat content (blue) for the last 25 ka. b, Comparison of EEI calculated from $\delta^{\rm I8}{\rm O}_{\rm benth}$ (ref. 21) (grey) with calculation with constraints from combined changes in ocean and latent heat content (blue) for the last 25 ka. c, Top of graph:

EEI calculated from δ^{18} O_{benth} (ref. 21) (grey, as in **b**) over the last 150 kiloyears. Intervals of positive EEI are marked with pink, and negative EEI are marked with blue. Dark-blue line shows summer solstice 65° N insolation⁴⁹. Bottom of graph: rate of relative sea level change (dRSL/dt) reconstructed from Red Sea planktonic δ^{18} O (ref. 35). Grey bars indicate Heinrich Stadial (H) intervals (as in ref. 21). Orange bars indicate H and YD during glacial terminations.

consistent with our reconstruction. In these simulations, the changes in ocean circulation lead to accumulation of heat in the ocean interior and warming concentrated in North Atlantic intermediate depths, which is driven by the disruption of deep convection and associated heat loss from the ocean to the atmosphere.

In addition to the oceanic response, Heinrich events are associated with Laurentide Ice Sheet mass wasting³¹, and thus latent heat gain. As high-resolution reconstructions of mean ocean temperature and coral-based sea level changes are mostly limited to the last 25,000 years, we cannot evaluate the relative contributions of ocean and latent heat to ΔE_{global} beyond this interval. However, marginal sea level reconstructions from planktonic δ^{18} O provide continuous constraints on relative sea level change, based on the control of sill depth on basin residence time and evaporation-driven enrichment in basin seawater δ^{18} O. In the absence of high-resolution coral-based constraints, we consult Red Sea records35 to assess whether the global energy gain during H intervals went, at least in part, into ice sheet melting. We note that there are well-documented differences between δ^{18} O-based constraints on ice volume—including the Red Sea record and geologic constraints for past intervals, including Marine Isotope Stage 3 (for example, refs. 36–38), so the following inferences should be considered with caution.

The Red Sea level reconstruction suggests that several of the larger Heinrich events are associated with high rates of sea level rise (Fig. 3c, refs. 35,39), which support a latent heat (in addition to ocean heat)

contribution to positive EEI during these intervals. Interestingly, the intensities of millennial-scale EEI peaks appear to be modulated by boreal summer insolation, which may reflect this high latitude control on ice sheet mass balance. Within the glacial, millennial-scale EEI maxima are briefer than those associated with the penultimate and last deglaciation and are mostly lesser in magnitude. However, the reconstructed EEI peak during H8 (87.6–85.1 ka) is comparable in magnitude to those of the last two deglaciations. Red Sea level records indicate that the rate of sea level rise during H8 is comparable to deglacial rates (albeit briefer), which may help explain this anomalously positive EEI within the glacial.

The reconstruction also suggests that the last and penultimate deglaciations both contain a double peak in EEI. In the last deglaciation, the two peaks are primarily related to the ocean heat gain across the two weak AMOC intervals of H1 and the YD 16,34 . In contrast, the penultimate deglaciation is marked by a single, prolonged weak AMOC interval (H11, 136–129 ka), so the double EEI peak across this interval is less readily explained. As continuous records of mean ocean temperature do not yet exist across the penultimate deglaciation, the rate and evolution of ocean heat uptake during this interval is unknown. Additionally, high-resolution coral-based reconstructions of sea level are not available for this interval, so rates of sea level rise (and thus the latent heat component of EEI) during this interval cannot be elucidated from these records. However, the Red Sea level record suggests two peaks in sea level rise rates which may, in part, explain the double peak in EEI across the penultimate deglaciation.

Mean ocean temperature and coral-based sea level reconstructions across the last interglacial (129–116 ka) suggest early interglacial ocean warmth coincident with higher sea level 40,41 , though the magnitude of the sea level anomaly, as well as its temporal evolution has been the subject of debate 42,43 . Mean ocean temperature decreases in the first few thousand years (-129–127 ka) of the interglacial, which, unless compensated by substantial ice sheet melting, would imply a negative EEI at the onset of this interglacial (Extended Data Fig. 5). However, the reconstructed EEI from $\delta^{18}{\rm O}_{\rm benth}$ suggests sustained, positive values until -126 ka. As discussed below, the implied inconsistency between agnostic and diagnostic EEI in the early last interglacial may be due to challenges in record alignment during earlier intervals.

Challenges and opportunities

The remarkable consistency between ice core, coral and sediment-based records across the last deglaciation not only reinforces early interpretations of $\delta^{\rm IS}{\rm O}_{\rm benth}$ records, but also demonstrates new ways in which they may be understood and utilized to quantitatively resolve past climate states. However, there are challenges in applying these techniques to earlier intervals related to dating and alignment of records from different archives. Absolute radiocarbon dating of sediment records is limited to the last -50 ka. Annual layer counting in ice cores may be possible in the shallower portion of a record but becomes increasingly difficult as layers thin with depth. Coral-based sea level records may be U–Th dated. However, corals provide discrete, rather than continuous markers of past sea level, and these markers become sparser further back in time.

While challenges exist, new dating and alignment techniques are continually developed. Efforts are underway to extend continuous ice core records through the Mid-Pleistocene transition. These efforts bring renewed interest in developing techniques for the alignment of ice and sediment records in order to probe this enigmatic interval⁴⁴.

Additional challenges include constraining past $\delta^{18}O_{ice}$. This is particularly salient within and beyond the mid-Pleistocene transition, as global climate and ice sheet geometries (and thus $\delta^{18}O_{ice}$) may have substantially differed from the late Pleistocene⁴⁵.

As with many proxies, our understanding of $\delta^{18}O_{benth}$ has evolved since its conception. This study takes the opportunity to assess this understanding using independent constraints on ice sheet volume and ocean temperature for the last 25,000 years. The findings are encouraging; while ocean temperature and ice volume trends are distinct, sediment records reliably record their combined contribution to $\delta^{18}O_{benth}$ across the last deglaciation. Ice volume accounts for a larger proportion of the net LGM-to-Holocene $\delta^{18}O_{benth}$ change, but the highest rates of $\delta^{18}O_{benth}$ change are largely driven by strong ocean warming during reduced AMOC intervals.

While early debates on the interpretation of $\delta^{18}O_{benth}$ records focused on the primary source of the signal, we find that—in the context of global energy change—the partitioning of $\delta^{18}O_{benth}$ into ocean temperature and ice volume is immaterial. As the oceans and ice sheets are, by far, the largest global energy reservoirs on ice age timescales, we demonstrate that $\delta^{18}O_{benth}$ traces ΔE_{global} and can be used to agnostically reconstruct EEI. As in the last deglaciation, we find millennial-scale variations in EEI throughout the last glacial cycle, with maxima during H intervals. While the North Atlantic is the centre of action for these intervals, their impacts are felt globally, and include large-scale restructuring of oceanic and atmospheric circulation $^{31,46-48}$. Understanding the nature of these millennial-scale perturbations to the global energy budget may therefore provide key insight into the slow feedbacks of our climate system.

Online content

Any methods, additional references, Nature Portfolio reporting summaries, source data, extended data, supplementary information, acknowledgements, peer review information; details of author contributions

and competing interests; and statements of data and code availability are available at https://doi.org/10.1038/s41561-023-01250-y.

References

- Zachos, J., Pagani, H., Sloan, L., Thomas, E. & Billups, K. Trends, rhythms, and aberrations in global climate 65 Ma to present. Science 292, 686–693 (2001).
- Friedrich, O., Norris, R. D. & Erbacher, J. Evolution of middle to late Cretaceous oceans—a 55 m.y. record of Earth's temperature and carbon cycle. Geology 40, 107–110 (2012).
- 3. Emiliani, C. Pleistocene temperatures. J. Geol. 63, 538-578 (1955).
- Shackleton, N. Oxygen isotope analyses and pleistocene temperatures re-assessed. *Nature* 215, 15–17 (1967).
- McDuff, R. E. The chemistry of interstitial waters from the upper ocean crust, site 395, Deep Sea Drilling Project Leg 78B. In *Initial* Reports of the Deep Sea Drilling Project 86 (eds Heath, G. R. et al.) 675–687 (U.S. Government Printing Office, 1984).
- Schrag, D. P. et al. The oxygen isotopic composition of seawater during the Last Glacial Maximum. Quat. Sci. Rev. 21, 331–342 (2002).
- Shackleton, N. J. The 100,000-year ice-age cycle identified and found to lag temperature, carbon dioxide, and orbital eccentricity. Science 289, 1897–1902 (2000).
- Waelbroeck, C. et al. Sea-level and deep water temperature changes derived from benthic foraminifera isotopic records. Quat. Sci. Rev. 21, 295–305 (2002).
- Cutler, K. B. et al. Rapid sea-level fall and deep-ocean temperature change since the last interglacial period. *Earth Planet. Sci. Lett.* 206, 253–271 (2003).
- Bintanja, R., Van De Wal, R. S. W. & Oerlemans, J. Modelled atmospheric temperatures and global sea levels over the past million years. *Nature* 437, 125–128 (2005).
- Elderfield, H. et al. Evolution of ocean temperature and ice volume through the mid-Pleistocene climate transition. Science 337, 704–709 (2012).
- Shakun, J. D., Lea, D. W., Lisiecki, L. E. & Raymo, M. E. An 800-kyr record of global surface ocean δ18O and implications for ice volume-temperature coupling. *Earth Planet. Sci. Lett.* 426, 58–68 (2015).
- 13. Rohling, E. J. et al. Sea level and deep-sea temperature reconstructions suggest quasi-stable states and critical transitions over the past 40 million years. *Sci. Adv.* **7**, 5326–5351 (2021).
- von Schuckmann, K. et al. Heat stored in the Earth system: where does the energy go? Earth Syst. Sci. Data 12, 2013–2041 (2020).
- Hansen, J. et al. Climate change: Earth's energy imbalance: confirmation and implications. Science 308, 1431–1435 (2005).
- Baggenstos, D. et al. Earth's radiative imbalance from the Last Glacial Maximum to the present. Proc. Natl Acad. Sci. USA 116, 14881–14886 (2019).
- Lambeck, K., Rouby, H., Purcell, A., Sun, Y. & Sambridge, M. Sea level and global ice volumes from the Last Glacial Maximum to the Holocene. Proc. Natl Acad. Sci. USA 111, 15296–15303 (2014).
- Bereiter, B., Shackleton, S., Baggenstos, D., Kawamura, K. & Severinghaus, J. Mean global ocean temperatures during the last glacial transition. *Nature* 553, 39–44 (2018).
- 19. Headly, M. A. & Severinghaus, J. P. A method to measure Kr/N_2 ratios in air bubbles trapped in ice cores and its application in reconstructing past mean ocean temperature. *J. Geophys. Res.* **112**, D19105 (2007).
- Shackleton, S. et al. Is the noble gas-based rate of ocean warming during the Younger Dryas overestimated? *Geophys. Res. Lett.* 46, 5928–5936 (2019).
- Lisiecki, L. E. & Stern, J. V. Regional and global benthic δ¹⁸O stacks for the last glacial cycle. *Paleoceanography* 31, 1368–1394 (2016).

- Oerlemans, J. Glacial cycles and ice-sheet modelling. Clim. Change 4, 353–374 (1982).
- Osman, M. B. et al. Globally resolved surface temperatures since the Last Glacial Maximum. *Nature* 599, 239–244 (2021).
- Hamme, R. C. & Severinghaus, J. P. Trace gas disequilibria during deep-water formation. *Deep Sea Res. Part I Oceanogr. Res. Pap.* 54, 939–950 (2007).
- Pöppelmeier, F. et al. The effect of past saturation changes on noble gas reconstructions of mean ocean temperature. Geophys. Res. Lett. 50, e2022GL102055 (2023).
- Austermann, J., Mitrovica, J. X., Latychev, K. & Milne, G. A. Barbados-based estimate of ice volume at Last Glacial Maximum affected by subducted plate. *Nat. Geosci.* 6, 553–557 (2013).
- Simms, A. R., Lisiecki, L., Gebbie, G., Whitehouse, P. L. & Clark, J. F. Balancing the last glacial maximum (LGM) sea-level budget. Quat. Sci. Rev. 205, 143–153 (2019).
- Yokoyama, Y., Lambeck, K., De Deckker, P., Johnston, P. & Fifield, L. K. Timing of the Last Glacial Maximum from observed sea-level minima. *Nature* 406, 713–716 (2000).
- Yokoyama, Y. et al. Rapid glaciation and a two-step sea level plunge into the Last Glacial Maximum. Nature 559, 603–607 (2018).
- Poirier, R. K. et al. Quantifying diagenesis, contributing factors, and resulting isotopic bias in benthic foraminifera using the foraminiferal preservation index: implications for geochemical proxy records. *Paleoceanogr. Paleoclimatol.* 36, e2020PA004110 (2021).
- 31. Hemming, S. R. Heinrich events: massive late Pleistocene detritus layers of the North Atlantic and their global climate imprint. *Rev. Geophys.* **42**, RG1005 (2004).
- Bohm, E. et al. Strong and deep Atlantic meridional overturning circulation during the last glacial cycle. *Nature* https://doi.org/ 10.1038/nature14059 (2015).
- Vidal, L. et al. Evidence for changes in the North Atlantic Deep Water linked to meltwater surges during the Heinrich events. Earth Planet. Sci. Lett. 146, 13–27 (1997).
- Galbraith, E. D., Merlis, T. M. & Palter, J. B. Destabilization of glacial climate by the radiative impact of Atlantic Meridional Overturning Circulation disruptions. *Geophys. Res. Lett.* 43, 8214–8221 (2016).
- Grant, K. M. et al. Rapid coupling between ice volume and polar temperature over the past 150,000 years. Nature 491, 744-747 (2012).
- Dalton, A. S. et al. The marine δ18O record overestimates continental ice volume during Marine Isotope Stage 3. Glob. Planet. Change 212, 103814 (2022).
- de Gelder, G. et al. High interstadial sea levels over the past 420ka from the Huon Peninsula, Papua New Guinea. Commun. Earth Environ. 3, 256 (2022).

- Pico, T. Toward new and independent constraints on global mean sea-level highstands during the Last Glaciation (Marine Isotope Stage 3, 5a, and 5c). *Paleoceanogr. Paleoclimatol.* 37, e2022PA004560 (2022).
- Yokoyama, Y., Esat, T. M. & Lambeck, K. Coupled climate and sea-level changes deduced from Huon Peninsula coral terraces of the last ice age. Earth Planet. Sci. Lett. 193, 579–587 (2001).
- 40. Shackleton, S. et al. Global ocean heat content in the Last Interglacial. *Nat. Geosci.* **13**, 77–81 (2020).
- Dutton, A., Webster, J. M., Zwartz, D., Lambeck, K. & Wohlfarth, B. Tropical tales of polar ice: evidence of Last Interglacial polar ice sheet retreat recorded by fossil reefs of the granitic Seychelles islands. Quat. Sci. Rev. 107, 182–196 (2015).
- O'Leary, M. J. et al. Ice sheet collapse following a prolonged period of stable sea level during the last interglacial. *Nat. Geosci.* 6, 796–800 (2013).
- 43. Dyer, B. et al. Sea-level trends across The Bahamas constrain peak last interglacial ice melt. *Proc. Natl Acad. Sci. USA* **118**, e2026839118 (2021).
- 44. Wolff, E. W., Fischer, H., van Ommen, T. & Hodell, D. A. Stratigraphic templates for ice core records of the past 1.5 Myr. *Clim* **18**, 1563–1577 (2022).
- Clark, P. U. & Pollard, D. Origin of the Middle Pleistocene Transition by ice sheet erosion of regolith. *Paleoceanography* 13, 1–9 (1998).
- Rhodes, R. H. et al. Enhanced tropical methane production in response to iceberg discharge in the North Atlantic. Science 348, 1016–1019 (2015).
- 47. Broecker, W. S. Massive iceberg discharges as triggers for global climate change. *Nature* **372**, 421–424 (1994).
- Cheng, H. et al. The Asian monsoon over the past 640,000 years and ice age terminations. *Nature* 534, 640–646 (2016).
- 49. Berger, A. & Loutre, M. F. Insolation values for the climate of the last 10 million years. *Quat. Sci. Rev.* **10**, 297–317 (1991).

Publisher's note Springer Nature remains neutral with regard to jurisdictional claims in published maps and institutional affiliations.

Springer Nature or its licensor (e.g. a society or other partner) holds exclusive rights to this article under a publishing agreement with the author(s) or other rightsholder(s); author self-archiving of the accepted manuscript version of this article is solely governed by the terms of such publishing agreement and applicable law.

© The Author(s), under exclusive licence to Springer Nature Limited 2023

Methods

Mean ocean temperature reconstruction from published ice core Kr/N₂, Xe/N₂ and Xe/Kr

To calculate the ocean temperature component of $\delta^{18}O_{benth}$ we first compile all published atmospheric noble gas ratio (Kr/N₂, Xe/N₂ and Xe/Kr) reconstructions covering the last 25,000 years (n=118, refs. 16,18,20,40). A 25 ka cut-offis chosen so as to exclude EPICA Dome C (EDC) ice samples within the bubble clathrate transition zone, which may not provide reliable noble gas data ^{16,50}. Samples from other records (WAIS Divide, or WDC, and Taylor Glacier, or TG) do not extend beyond 25 ka. All data are kept on the age models from their original publications (AICC2012 for EDC, and WD2014 for WDC and TG).

The measured noble gas ratios in ice cores must be corrected for gas fractionation in the firn to derive the atmospheric ratios¹⁹. In this study, we use the published fractionation-corrected noble gas ratios from each study, except in the case of TG samples from ref. 40 (n = 10), for which we apply the correction of ref. 20, so that all samples from the same ice core are corrected using the same method. In the case of the EDC data¹⁶, the atmospheric noble gas ratios are reported using two methods of fractionation correction. Here we use the dataset that includes correction for kinetic fractionation. Comparison of the differing methods of firn fractionations are explored in the original publications, as well as ref. 51. To compute mean ocean temperature from the corrected noble gas ratios, we report these gas ratios relative to their late Holocene (0-5 ka) average for the cores with data from this interval (EDC and WDC). In the case of TG, no data are available from this interval, so we report these ratios relative to a modern atmosphere standard.

To calculate mean ocean temperature from the atmospheric noble gas ratios, we employ the ocean–atmosphere box model of ref. 18. In brief, the box model is composed of a one-box atmosphere and three-box ocean. The relative temperatures, salinities and volumes of the ocean boxes are assigned on the basis of the temperature and salinity distributions of the modern ocean. However, using a one-box ocean yields nearly identical results 18 . The model computes the Xe, Kr and $\rm N_2$ in each reservoir on the basis of the respective volumes and the temperatures and salinities of each ocean box. The model is then inverted to solve for the required ocean temperature change to match the reconstructed palaeo-atmospheric noble gas ratios.

Ocean volume, salinity and the atmospheric pressure at sea level all influence the partitioning of gases between the ocean and atmosphere, and thus the atmospheric noble gas ratios. To account for these affects and how they vary in time, we apply the ref. 17 sea level curve (and reported uncertainties) to our box model calculations. All box model parameterizations are the same as prescribed in ref. 18, with the exception that we make no assumption about a time-varying noble gas saturation state. This is later explored in the 'Disagreement in LGM $\Delta\delta^{\rm 18}{\rm O}$ ' section. In addition, we apply the updated solubility curves of ref. 52 in our box model calculations.

From the three atmospheric noble gas ratios (Kr/N_2 , Xe/N_2 and Xe/Kr), we get three evaluations of mean ocean temperature for each sample. As in previous work, we report the average of the three results. To assess uncertainties in these mean ocean temperature reconstructions, we create 10,000 Monte Carlo realizations of each corrected noble gas ratio (n=118 samples $\times 3$ noble gas ratios) from their published uncertainties, and 10,000 realizations of the sea level curve from its reported uncertainty to run through our box model routine. As above, we average the three results from the noble gas ratios to produce 10,000 mean ocean temperature realizations of the 118 datapoints.

Calculation of ocean temperature and ice volume contribution to $\delta^{18}O_{benth}$ and comparison with the $\delta^{18}O_{benth}$ compilation

To compare ocean temperature, ice volume and $\delta^{18}O_{benth}$ reconstructions, we create splined versions of each record, along with estimates

of uncertainties. To produce a splined mean ocean temperature record, bootstrapped timeseries are produced by randomly sampling with replacement from the 10,000 Monte Carlo realizations of the 118 noble gas samples. We fit each of these timeseries to a spline with a 2,500 year cut-off period using the MATLAB 'csaps' function. A 2,500 year cut-off period was chosen, as in ref. 16, to minimize the influence of analytical noise, while still capturing millennial-scale features that may also be recorded in the lower-resolution $\delta^{18}O_{benth}$ record. The 10,000 splines are averaged to produce a final, smoothed ocean temperature record, along with uncertainties. These records are then used to calculate temperature-driven changes in global $\delta^{18}O_{benth}$ with the quadratic formula of the ref. 53 palaeotemperature equation ($T=0.1\times\delta^{18}O^2-4.38\times\delta^{18}O+16.9$) assuming a late Holocene (0–5 ka) mean ocean temperature of 3.53 °C (ref. 54).

We apply the deglacial sea level reconstruction of ref. 17 to calculate the ice volume component of $\delta^{18}O_{benth}$, which incorporates corals and coastal sediment constraints on relative sea level with glacial isostatic adjustment models to reconstruct eustatic sea level. A splined version of the sea level record is used in this calculation, produced using the same method as the mean ocean temperature spline described above. The smoothing applied to produce the spline means that submillennial sea level changes (such as in Meltwater Pulse 1A) are not well resolved. However, such short-term features are unlikely to be well captured in global $\delta^{18}O_{benth}$. While the thermosteric component of sea level change is relatively small, we may account for and remove this signal from the total sea level change (to isolate the ice volume component) using our mean ocean temperature spline scaled to the total LGM-to-Holocene thermosteric sea level change $(2.4 \pm 0.3 \text{ m (ref. } 27))$. We also consider the eustatic sea level reconstruction derived from fossil coral records from the Great Barrier Reef 29 to calculate the ice volume component of $\delta^{18}O_{benth}$ applying the same methods as above.

To calculate the $\delta^{18}O_{benth}$ changes due to ice volume changes we rearrange the equation of ref. 9: $\Delta\delta^{18}O = \delta^{18}O_{ice}/(D/\Delta SL-1)$, where $\delta^{18}O_{ice}$ is the mean ice sheet $\delta^{18}O$ ($-30\pm2\%$), D is the modern mean ocean depth of 3,682.2 m (ref. 55), and ΔSL is the eustatic sea level anomaly relative to modern. In our calculations, this mean $\delta^{18}O_{ice}$ value applies to the ice that contributes to global ice volume change (and thus the change in seawater $\delta^{18}O$) and does not include extant ice sheets. We note that this method of estimating the sea level contribution to global $\delta^{18}O_{benth}$ neglects the influence of ocean bathymetry. Changes in the volume of floating ice shelves represent another source of uncertainty, as this influences the volume of water stored as ice (and thus seawater $\delta^{18}O$) without any change in sea level.

The sum of the ocean temperature and ice volume components of $\delta^{18}O_{benth}$ ($\Delta\delta^{18}O_{predicted}$) from ocean temperature and sea level reconstructions are compared with the global $\delta^{18}O_{benth}$ compilation of ref. 21. For this comparison, a splined version of the $\delta^{18}O_{\text{benth}}$ compilation was produced using the same method applied to the ocean temperature and sea level reconstructions. As the global $\delta^{18}O_{\text{benth}}$ stack averages over hundreds of individual records, we do not employ bootstrapping to produce the global $\delta^{18}O_{\text{benth}}$ spline. Because the stack is produced by binning individual records into 500 year intervals, we randomly perturb the age model of the global $\delta^{18}O_{\text{benth}}$ stack within its 500 year binning in our Monte Carlo realizations to incorporate effects of age uncertainty and smoothing associated with this binning in the global $\delta^{18}O_{benth}$ spline. LGM and deglacial anomalies $(\Delta \delta^{18}O)$ are reported relative to the late Holocene average (0-5 ka), as sea level, ocean temperature and $\delta^{18}O_{benth}$ are effectively constant over this interval.

Calculation of global energy change and EEI from benthic δ^{18} O

To assess the conversion of $\delta^{18}O_{benth}$ to global energy change (ΔE_{global}) and EEI we assume that ocean heat content and ice sheet latent heat content changes are the dominant changes in global energy reservoirs

on ice age timescales. This assumption is based on the work of ref. 16, which evaluated the LGM-to-Holocene changes in global energy and found that changes in ocean heat content and ice sheet latent heat content are orders of magnitude larger than other global energy changes.

The primary goal of this section is to determine if we may use $\delta^{18}O_{benth}$ to agnostically reconstruct ΔE_{global} and EEI. That is, we calculate ΔE_{global} under the assumption that changes in global $\delta^{18}O_{benth}$ are driven entirely by changes in (1) ice sheet volume or (2) entirely by ocean temperature (Extended Data Fig. 3). If they differ, we must deconstruct $\delta^{18}O_{benth}$ into its ice volume and ocean temperature components to calculate ΔE_{global} and EEI. However, if they are similar, there is no need to deconstruct benthic $\delta^{18}O_{;}$ it may be directly converted to ΔE_{global} and EEI without accurate knowledge of the reservoir of energy gain/loss (ocean heat content or latent heat content).

To calculate ice sheet latent heat content changes from global $\Delta \delta^{18}$ O_{benth}, we calculate the change in sea level per equivalent change in δ^{18} O_{benth}: Δ SL = $D/(\Delta\delta^{18}$ O_{ice}/ $\Delta\delta^{18}$ O + 1). Here we are assuming that the entire $\delta^{18}O_{benth}$ change ($\Delta\delta^{18}O$) is due to ice volume changes to probe how sensitive our global energy reconstructions are to assumptions about the partitioning of $\delta^{\rm 18}O_{\rm benth}$ into ocean temperature and ice volume changes. As in the previous section we apply a mean $\delta^{18}O_{ice}$ of $-30 \pm 2\%$ (the sensitivity of these calculations to the applied δ^{18} O_{ice} is shown in Extended Data Fig. 4). The associated energy change is then calculated as in ref. 16. Briefly, the sea level change is converted to a freshwater mass change using the modern ocean area 361.84 × 106 km² (ref. 55) and freshwater density and then multiplied by the latent heat of fusion of freshwater. This energy change is then increased by an additional $10 \pm 5\%$ to account for the energy required to warm the ice to the melting point (assuming a mean ice sheet temperature of -20 °C). Global energy imbalance is then calculated by taking the time derivative of this reconstructed $\Delta E_{\rm global}$ and dividing it by Earth's surface area.

To calculate ocean heat content changes from global $\delta^{18}O_{benth}$, we calculate ocean temperature from global $\delta^{18}O_{benth}$ using the ref. 53 palaeotemperature equation (see previous section). Here we are assuming that the $\delta^{18}O_{benth}$ signal is entirely an ocean temperature signal. However, we enforce an absolute lower mean ocean temperature limit of -2 °C (the freezing point of seawater), so for any values of global $\delta^{18}O_{\text{benth}} > 4.85\%$, we assume that the remainder of the $\delta^{18}O$ signal is due to an ice volume change and calculate the associated latent heat change as above. In this case, it is very unlikely that the entire $\delta^{18}O_{henth}$ signal is due to the equilibrium isotope effect. However, the purpose of this exercise is to evaluate the possible range of ΔE_{global} from $\delta^{18}O_{benth}$. From the global $\delta^{18}O_{benth}$ calculation of mean ocean temperature, we then calculate ΔE_{global} using the modern ocean volume 1.3324 × 10⁹ km³ (ref. 55) multiplied by the average density and temperature-dependent specific heat of seawater. As above, global energy imbalance is then calculated by taking the time derivative of ΔE_{global} and dividing it by Earth's surface area.

From these two extreme assumptions in the partitioning of $\delta^{18}O_{benth}$ (entirely ice volume or entirely ocean temperature) used to calculate ΔE_{global} and EEI, we find that the total energy changes agree within -20%. Therefore, an accurate partitioning of $\delta^{18}O_{benth}$ into ocean temperature and ice volume changes is unnecessary in reconstructing EEI (Extended Data Fig. 3).

To produce $\Delta E_{\rm global}$ and EEI splines, 4,000 iterations of the ocean heat and 6,000 iterations of the latent heat calculations from $\delta^{18}O_{\rm benth}$, along with their uncertainties, are produced via Monte Carlo methods. These 10,000 global energy histories are then resampled via bootstrapping and splines (and their time derivatives) are produced applying a 2,500 year cut-off period using the MATLAB 'csaps' function. The 10,000 iterations of the global energy splines and time derivatives are then used to evaluate $\Delta E_{\rm global}$ and EEI, respectively, along with 1σ confidence envelopes for each record (Fig. 3a,b).

Data availability

File including the reconstructions from this study and original data used to produce reconstructions is available at https://doi.org/10.5281/zenodo.8237374.

References

- Bereiter, B., Kawamura, K. & Severinghaus, J. P. New methods for measuring atmospheric heavy noble gas isotope and elemental ratios in ice core samples. *Rapid Commun. Mass Spectrom.* 32, 801–814 (2018).
- 51. Haeberli, M. et al. Snapshots of mean ocean temperature over the last 700 000 years using noble gases in the EPICA Dome C ice core. *Clim. Past* **17**, 843–867 (2021).
- Jenkins, W. J., Lott, D. E. & Cahill, K. L. A determination of atmospheric helium, neon, argon, krypton, and xenon solubility concentrations in water and seawater. *Mar. Chem.* 211, 94–107 (2019).
- Shackleton, N. J. Attainment of isotopic equilibrium between ocean water and the benthonic foraminifera genus *Uvigerina*: isotopic changes in the ocean during the last glacial. *Colloq. Int. Cent. Natl Rech. Sci.* 219, 203–210 (1974).
- 54. Sarmiento, J. L. & Gruber, N. Ocean Biogeochemical Dynamics (Princeton Univ. Press, 2006).
- 55. Charette, M. & Smith, W. The volume of Earth's ocean. Oceanography 23, 112–114 (2010).

Acknowledgements

We thank M. Bender, J. Higgins and J. Severinghaus for helpful discussions and encouragement in pursuing this project. We are grateful to J. Severinghaus for pointing us to the Great Barrier Reef sea level reconstruction. Thanks to S. Hines for her expertise and advice on the interpretation of marine sediment records. The first author was supported by National Science Foundation awards 1744993 and 2052958. A.S. was supported by National Science Foundation award 2049359.

Author contributions

S.S. and D.B. designed the research. A.S. and S.S. established the method for splined reconstructions via Monte Carlo error propagation. D.B. and S.S. re-analysed the published noble gas records to produce the splined ocean temperature reconstruction. S.S., A.S., D.B. and L.E.L. analysed the data. S.S. wrote the paper with input from all authors.

Competing interests

The authors declare no competing interests.

Additional information

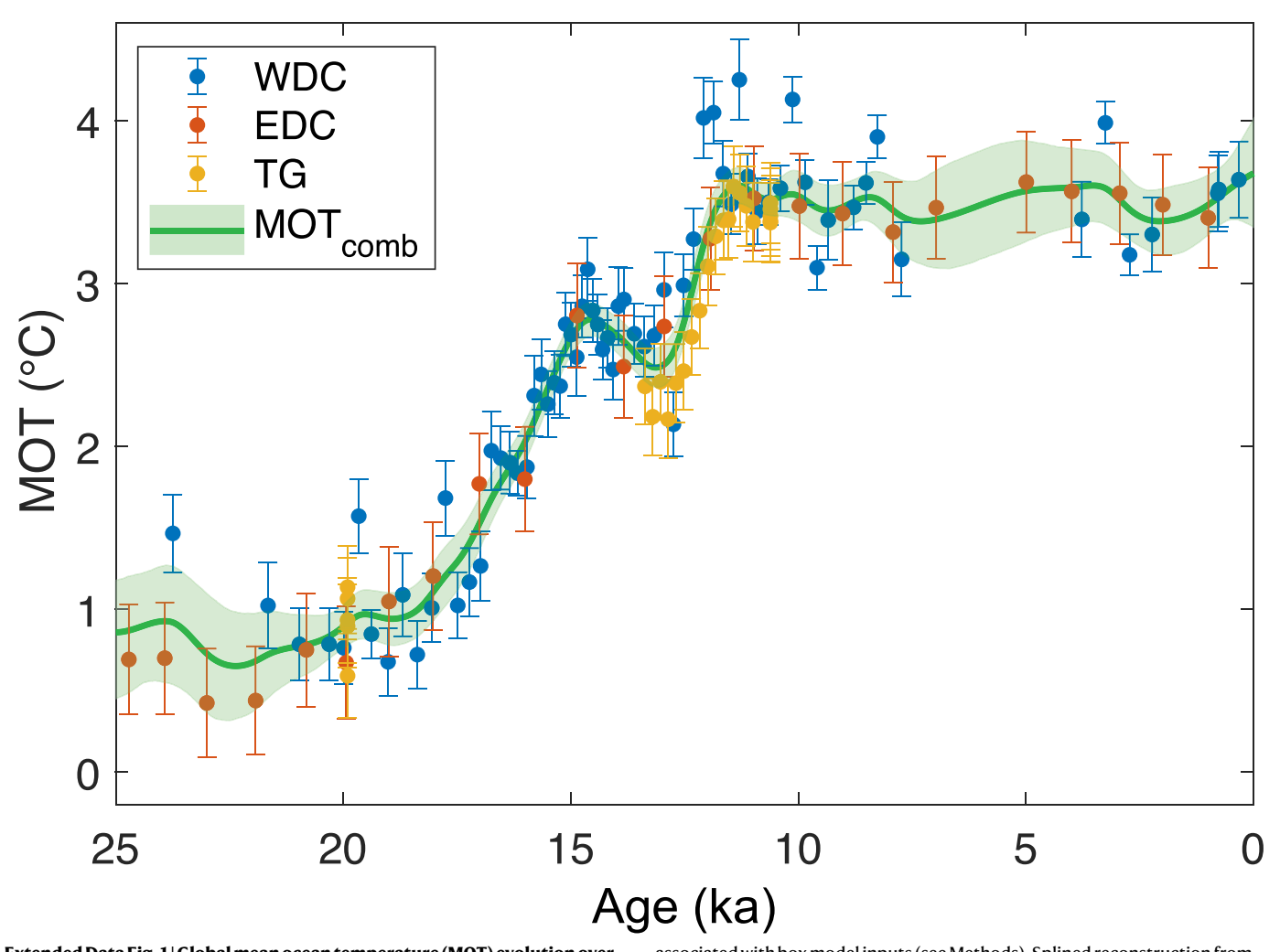
Extended data is available for this paper at https://doi.org/10.1038/s41561-023-01250-y.

Supplementary information The online version contains supplementary material available at https://doi.org/10.1038/s41561-023-01250-y.

Correspondence and requests for materials should be addressed to Sarah Shackleton.

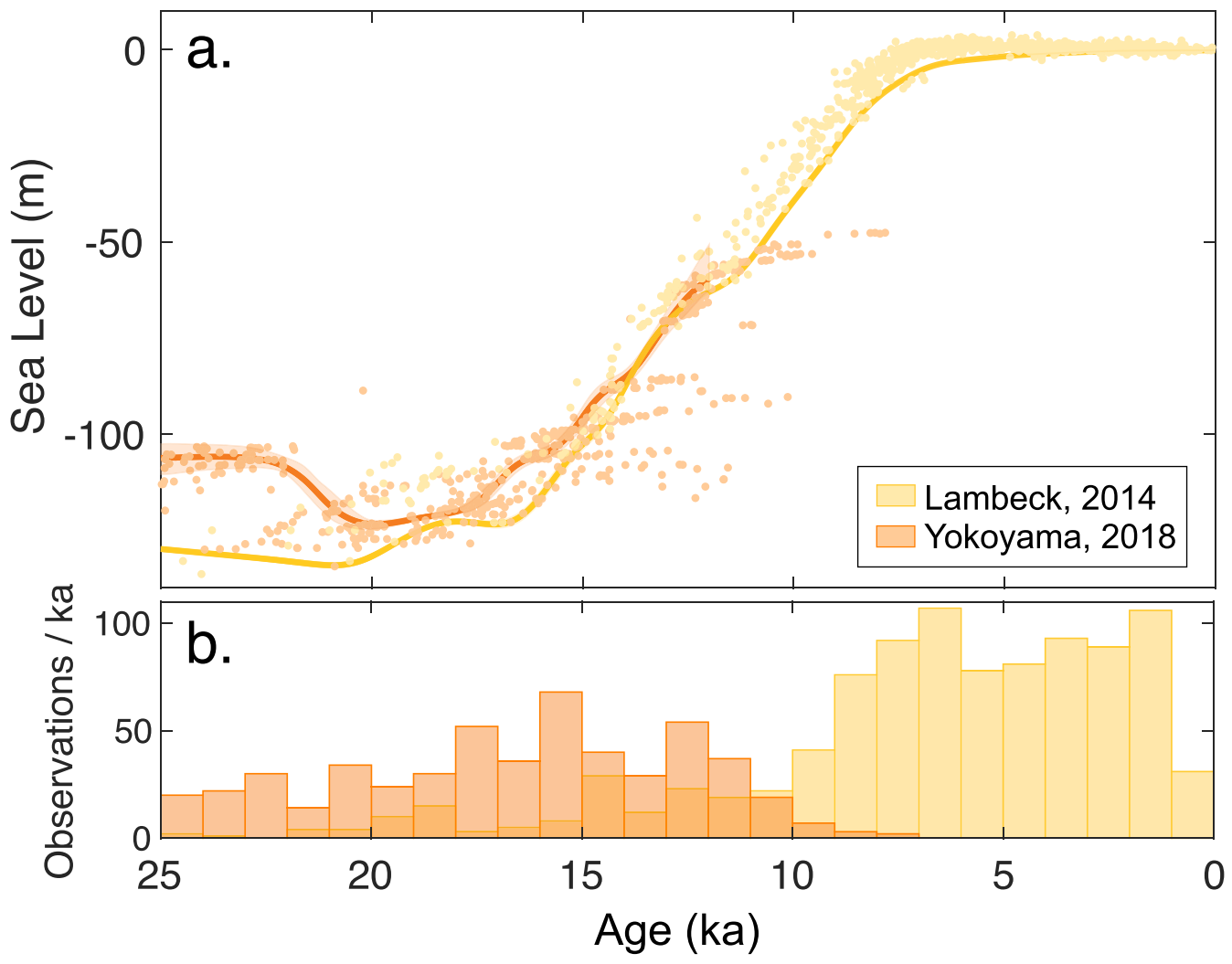
Peer review information *Nature Geoscience* thanks the anonymous reviewers for their contribution to the peer review of this work. Primary Handling Editor: James Super, in collaboration with the *Nature Geoscience* team.

Reprints and permissions information is available at www.nature.com/reprints.



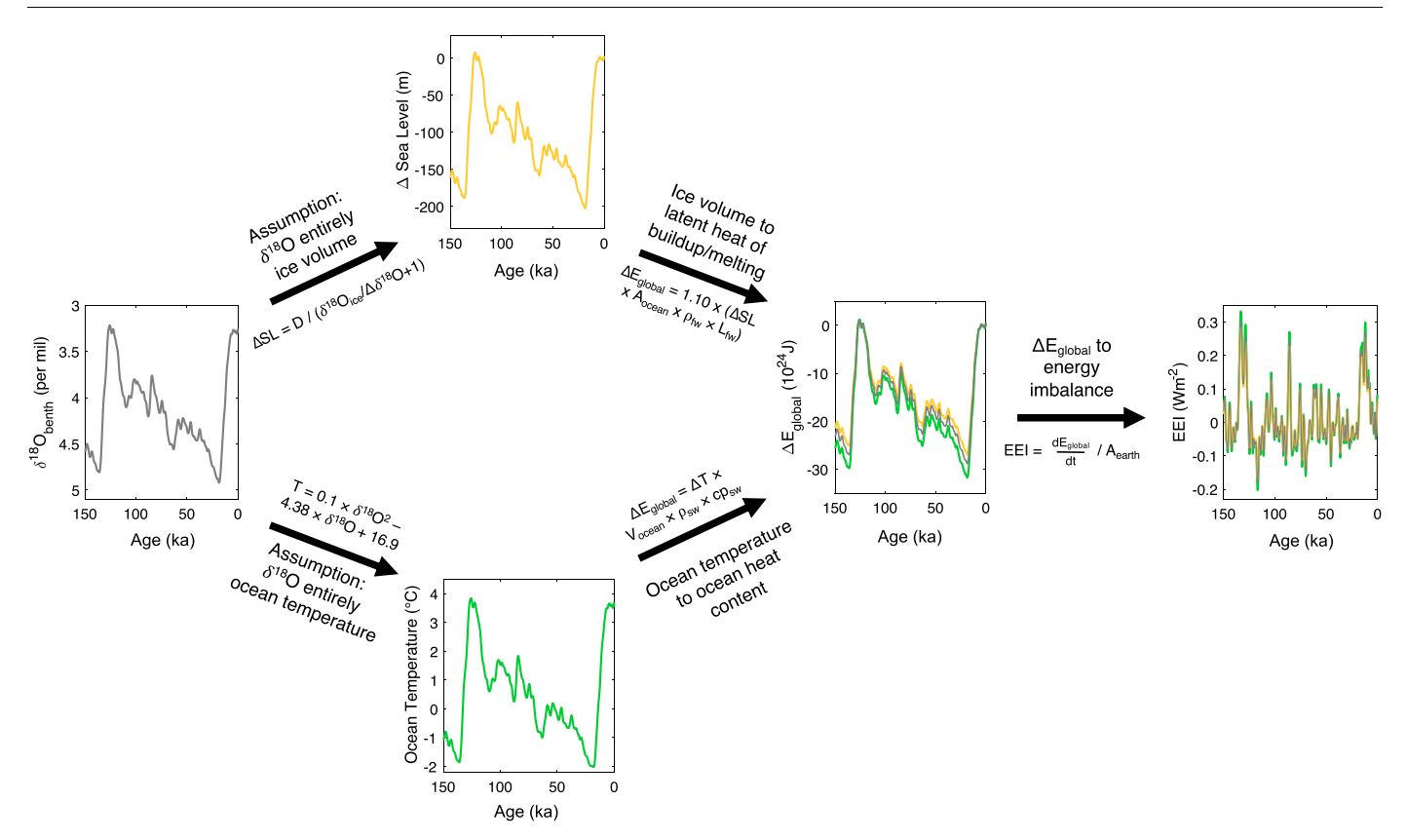
Extended Data Fig. 1 | Global mean ocean temperature (MOT) evolution over the last 25 ka. Individual samples from WAIS Divide 18 (WDC, blue), EPICA Dome C^{16} (EDC, red) and Taylor Glacier 20,40 (TG, yellow) are shown as points with 1σ error bars calculated from published analytical uncertainties and uncertainties

associated with box model inputs (see Methods). Splined reconstruction from these combined data (MOT $_{\rm comb}$) are shown in green with 1σ confidence envelope shown in shading centered on mean spline (solid line). Note that absolute mean ocean temperature (rather than temperature anomaly) is shown here.



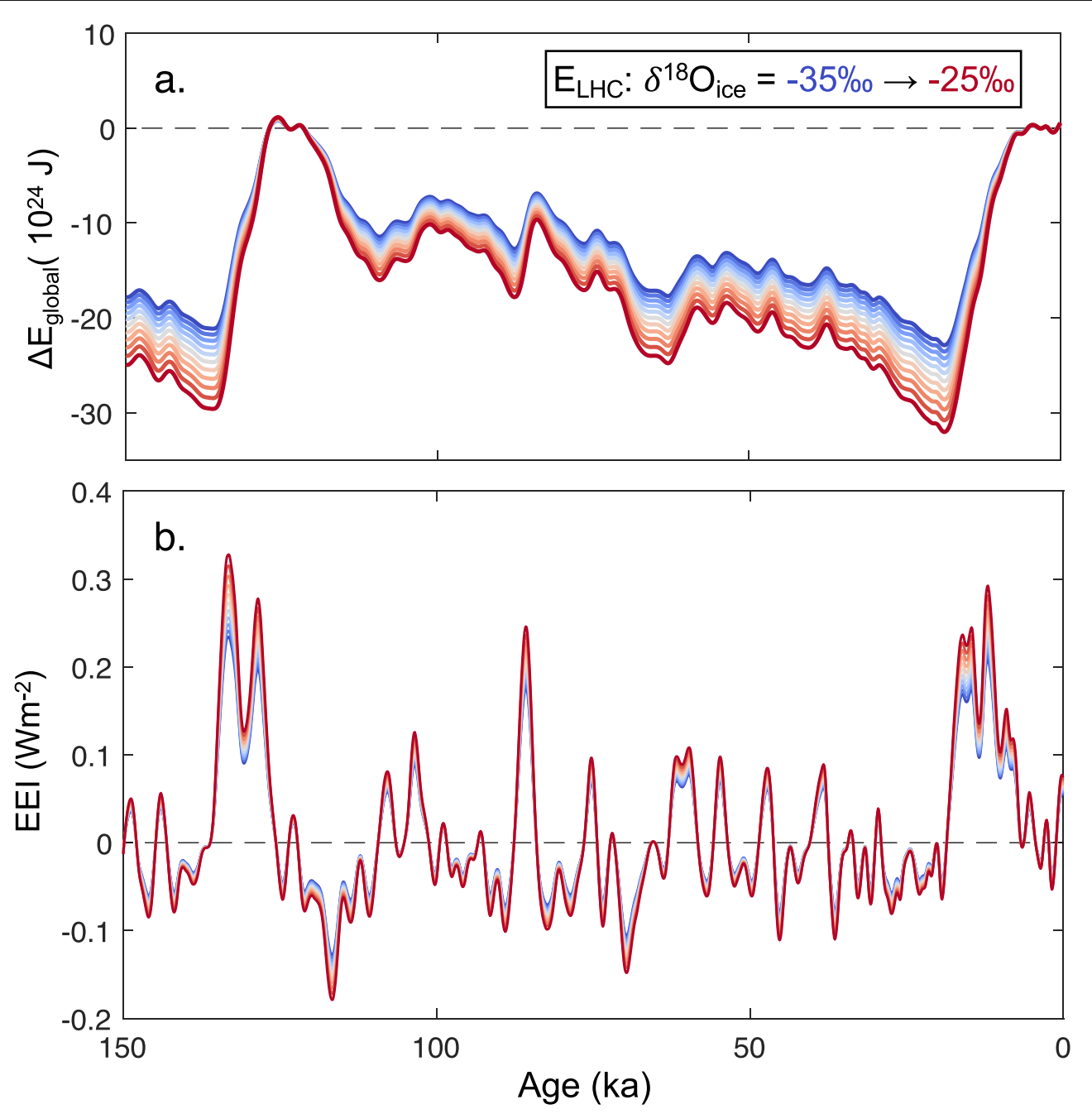
Extended Data Fig. 2 | Raw relative sea level data and calculated eustatic sea level curves considered in this study. In a) points represent the individual raw observations from refs. 17 (yellow) and²⁹ (orange) and solid lines show the

splines of the eustatic sea level curves from each study that are used to compute the ice volume component of $\delta^{18}O_{\text{benth}}.$ **b)** shows the number of raw sea level observations for each study per thousand-year bin.

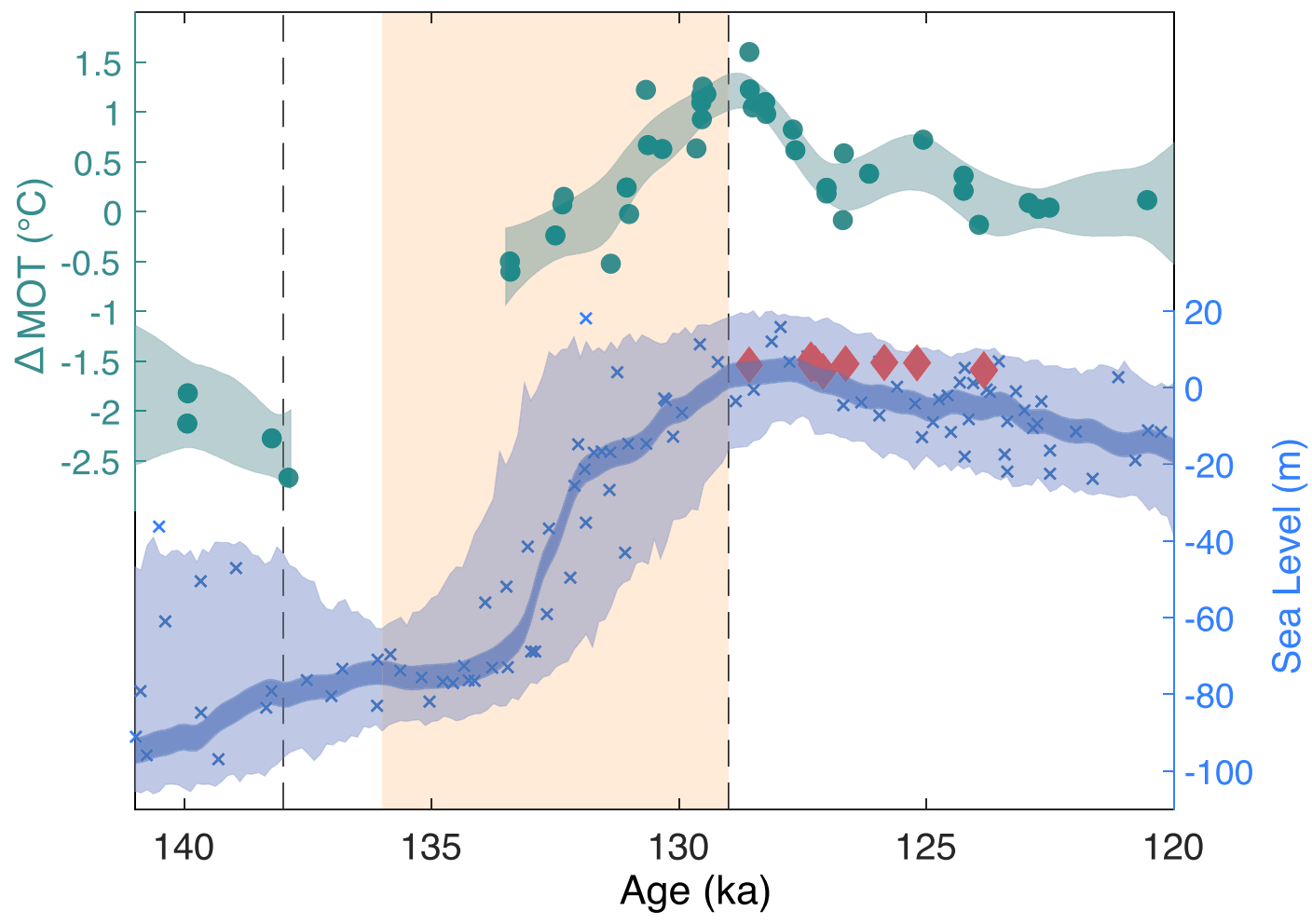


Extended Data Fig. 3 | Agnostic reconstruction of Earth's energy imbalance (EEI) from $\delta^{18}O_{benth}$. Here we outline the steps taken to calculate EEI from $\delta^{18}O_{benth}$ (left to right), which are described in detail in the methods. Briefly, $\delta^{18}O_{benth}^{21}$ (left) is converted into sea level (second panel, top in yellow) and ocean temperature (second panel, bottom in green) using the assumption that the $\delta^{18}O_{benth}$ signal is entirely attributed to one or the other. We then calculate the energy change associated with ice sheet buildup/melting from the sea level reconstruction

(third panel, yellow) and with ocean warming/cooling from the ocean temperature reconstruction (third panel, green). EEI is then calculated by taking the time derivative of the energy changes and averaging over Earth's surface area (panel 4). The gray lines in panels 3 and 4 show the calculated the global energy change ($\Delta E_{\rm global}$) and EEI if we assume a constant 60/40 split of $\delta^{\rm IS}O_{\rm benth}$ between ice volume and ocean temperature changes.



Extended Data Fig. 4 | Sensitivity of calculated (a) global energy change (ΔE_{global}) and (b) Earth's energy imbalance (EEI) to applied $\delta^{18}O_{ice}$. Here we assume the $\delta^{18}O_{bent}^{21}$ record is entirely an ice volume signal and calculate the energy change using a wide range of mean ice sheet $\delta^{18}O$ (-35% to -25%) to test the sensitivity of calculated EEI to this parameter.



Extended Data Fig. 5 | Mean ocean temperature 40 and sea level 35,41 reconstructions for Termination II and the Last Interglacial. Blue show sea level reconstructions from Red Sea plankonic δ^{18} O 35 and red diamonds show coral records from the Seychelles 41 . Dashed line indicates the onset and end of the termination and orange shading indicates the timing of Heinrich Stadial II.